

DIPR: Efficient Point Cloud Registration via Dynamic Iteration

Yang Ai¹

Qiang Bai¹

Jindong Li¹

Xi Yang^{1,2,3,*}

¹School of Artificial Intelligence, Jilin University,

²Engineering Research Center of Knowledge-Driven Human-Machine Intelligence, MoE, China,

³Key Laboratory of Ancient Chinese Script, Culture Relics and Artificial Intelligence, Jilin University
aiyangjlu21@gmail.com, {baiqiang23, jdli21}@mails.jlu.edu.cn, yangxi21@jlu.edu.cn

Abstract

Point cloud registration (PCR) is an essential task in 3D vision. Existing methods achieve increasingly higher accuracy. However, a large proportion of non-overlapping points in point cloud registration consume a lot of computational resources while negatively affecting registration accuracy. To overcome this challenge, we introduce a novel Efficient Point Cloud Registration via Dynamic Iteration framework, DIPR, that makes the neural network interactively focus on overlapping points based on sparser input points. We design global and local registration stages to achieve efficient course-to-fine processing. Beyond basic matching modules, we propose the Refined Nodes to narrow down the scope of overlapping points by using adopted density-based clustering to significantly reduce the computation amount. And our SC Classifier serves as an early-exit mechanism to terminate the registration process in time according to matching accuracy. Extensive experiments on multiple datasets show that our proposed approach achieves superior registration accuracy while significantly reducing computational time and GPU memory consumption compared to state-of-the-art methods.

Introduction

Point cloud registration (PCR), which aims to align two or more point sets within the same coordinate system, plays a crucial role in many fields such as autonomous driving and robotics. With the advancement of deep learning, researchers are working on extracting learning-based features to replace un-robust traditional hand-crafted descriptors, e.g. GeoTrans (Qin et al. 2022), RoITR (Yu et al. 2023b). However, due to the substantial data volume in practical scenarios, learning-based point cloud registrations tend to exhibit high time complexity and additional computational overhead. To address this problem, simple downsampling strategies, e.g., KPConv (Thomas et al. 2019), are employed in the existing methods, that select sparse points and their features from dense point clouds across hierarchical levels, and then pass them to an encoder for information interaction. However, this can result in numerous outliers (points in non-overlapping areas) during the registration process, which disrupt subsequent calculations for point feature pairing and unnecessarily consume significant computing resources, given that such downsamplings are typically global.

Starting from this observation, we introduce the spatial-wise dynamic network (Wang et al. 2020), a dynamic net-

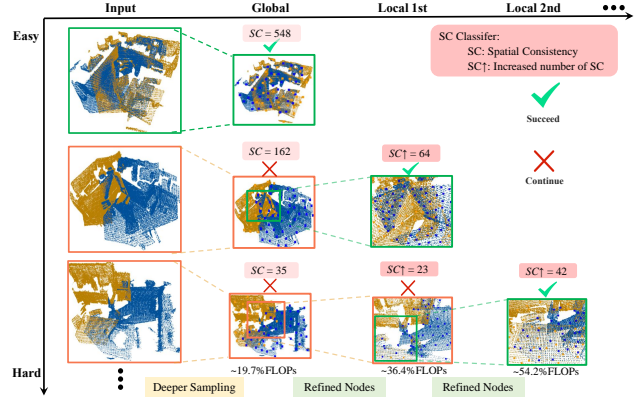


Figure 1: We propose a dynamic iteration approach to improve the accuracy and efficiency of PCR. Our DIPR samples sparser point clouds and dynamically search for overlapping areas in the local stage by Refined Nodes. After each stage, we design an SC Classifier to determine whether the registration result needs to be continued. Here, SC and $SC\uparrow$ are the registration evaluation metrics. “FLOPs” refers to the proportion of the computation required by our method versus RoITR (Yu et al. 2023b).

work that can adjust network structures and parameters based on data, into PCR tasks to reduce computation resources during inference. Although this approach was applied to 2D visual tasks, for 3D point clouds, the irregularity and larger scale of the data make managing spatial redundancy more challenging. Therefore, we propose a novel two-stage network with specifically designed Refined Nodes and spatial consistency-based SC Classifier to iteratively search regions within the inlier set, thus significantly reducing the computational cost of feature encoding.

As shown in Figure 1, our DIPR primarily consists of two stages. First is the global registration stage, where we employ sparse global sampling for candidate pair selection and perform coarse registration with sparser inputs. The input scenes with discriminative features can easily be correctly aligned with high accuracy and plenty of pairings in this stage. Then, for complex scenes, the global registration may fail to produce sufficient correspondences, and our network proceeds to the second stage to select regions within the inlier set. In this local registration stage, we design the

Refined Nodes for the paired points from global registration. This module incorporates a density-based clustering algorithm and a Cluster-centric Neighborhood Augmentation (CNA) module. The clustering algorithm is used to identify regions where paired points are densely clustered, while the CNA searches within these regions to form data for the subsequent registration phase. After each iteration, we also design a classifier based on spatial consistency to evaluate the registration performance based on dynamic thresholds and decide whether to proceed with the next iteration.

Different from other iteration-based point cloud registrations (Jiang et al. 2021; Yu et al. 2023c) and baselines (Wang et al. 2020; Qin et al. 2022; Yu et al. 2023b), our main contributions could be summarized as follows:

- We propose a novel efficient point cloud registration via dynamic iteration framework, DIPR, to dynamically discover the overlapping regions between point clouds, which effectively removes outliers and facilitates adaptive inference in the testing phase. To the best of our knowledge, we are the first to introduce the dynamic approach to improve the efficiency of PCR.
- We design a Refined Nodes module with a clustering algorithm to narrow down the registration region, efficiently reducing the computational load without introducing additional networks. We also design a SC Classifier to serve as the early-exit mechanism of iterations. These structures enable our network to efficiently extract features using sparser input points (Deeper Sampling).
- We conduct comprehensive experiments on multiple public datasets (3DMatch, 3DLoMatch, KITTI), demonstrating our DIPR achieves state-of-the-art performance while achieving time and computational efficiency advantages over existing methods.

Related Work

Correspondence-based Methods

Traditional methods extract correspondences between two point clouds based on feature descriptors and predict the transformation matrix based on paired points (Chen, Yang, and Tao 2022; Xu et al. 2022). Recently, many variants (Fragoso et al. 2013; Yang, Shi, and Carlone 2020) propose using outlier removal to improve the accuracy of correspondences. PointDSC (Bai et al. 2021) and SC²-PCR (Chen et al. 2022) proposes the outlier rejection module by introducing deep spatial consistency and global consistency to measure the similarity between correspondences. Although these methods (Shen et al. 2022; Huang et al. 2024) have made significant progress, they are all greatly affected by initial correspondence. In comparison, our work insights by the idea of dynamically selecting matching points to improve the accuracy of correspondences.

Deep-learned Feature Descriptors

The feature descriptor in the PCR is used to extract features to construct correspondences. Compared with traditional hand-crafted descriptors such as (Rusu et al. 2009; Chu and Nie 2011), 3DMatch (Zeng et al. 2017) learns 3D

geometric features to convert local patches into voxel representations. In recent years, more and more works (Zhang et al. 2022; Yu et al. 2022) focus on the low overlap problems. Predator (Huang, Gojcic, and Schindler) extracts low-overlap point clouds dataset to form 3DLoMatch and uses the cross-attention module to interact with the point clouds to build feature descriptors. GeoTrans (Qin et al. 2022) and other papers (Yu et al. 2023b) learn more geometric features to improve the robustness of PCR and achieves high accuracy. These methods compute features for each point and its neighborhood, resulting in an unavoidably large amount of computation. Recently, many of the methods have used additional information to improve the PCR process, such as (Yu et al. 2023c; Chen et al. 2024a,b).

However, these methods are challenging to implement in real-world scenarios due to their complexity and high resource demands. In comparison, our method uses sparser sampling in the down-sampling stage to reduce the consumption of computational resources.

Dynamic Neural Networks

The dynamic neural network is a structure that dynamically changes based on computational resources and input data. Our approach is mainly related to spatial-wise (Zhou et al. 2016) dynamic networks which exploit spatial redundancy to improve efficiency. Mobilenet (Howard et al. 2017) observes that a low resolution might be sufficient for most "easy" samples and exploits feature solutions to remove redundancy. Besides, early-exiting mechanism (Li et al. 2019; Yu et al. 2023a) is widely studied and used to decide whether the network continues. GFNet (Wang et al. 2020) imitates the visual system of the human eye and processes an observation process from a global glance to a local focus to search more critical regions. Based on GFNet, we propose a coarse-to-fine feature learning approach combined with registration evaluation to adjust the registration range.

Method

Given a pair of 3D point clouds $P_X = \{p_{x_i} \in \mathbb{R}^3 \mid i = 1, \dots, N\}$ and $P_Y = \{p_{y_i} \in \mathbb{R}^3 \mid i = 1, \dots, M\}$, the purpose of our task is to estimate a rigid transformation $SE(3)$ which aligns the point clouds X and Y with a rotation matrix $R \in SO(3)$ and a translation $T \in \mathbb{R}^3$. Figure 2 shows the overview of our method.

Our method is divided into two parts, namely the global registration stage and the local registration stage. In the global stage, we first employ the Deeper Sampling to perform multi-scale deep sampling on the input point clouds and extract initial features of each point. Basic Matching module is employed to conduct coarse-grained registration of the data. For the local registration stage, we employ the Refined Nodes module to get the overlapping area based on the previous registration result and start the next registration. After every registration stage, the SC Classifier is designed to judge whether the results meet the accuracy requirements.

Global Registration

In the global registration stage, we aim to align the entire point cloud by using a hierarchical approach. This pro-

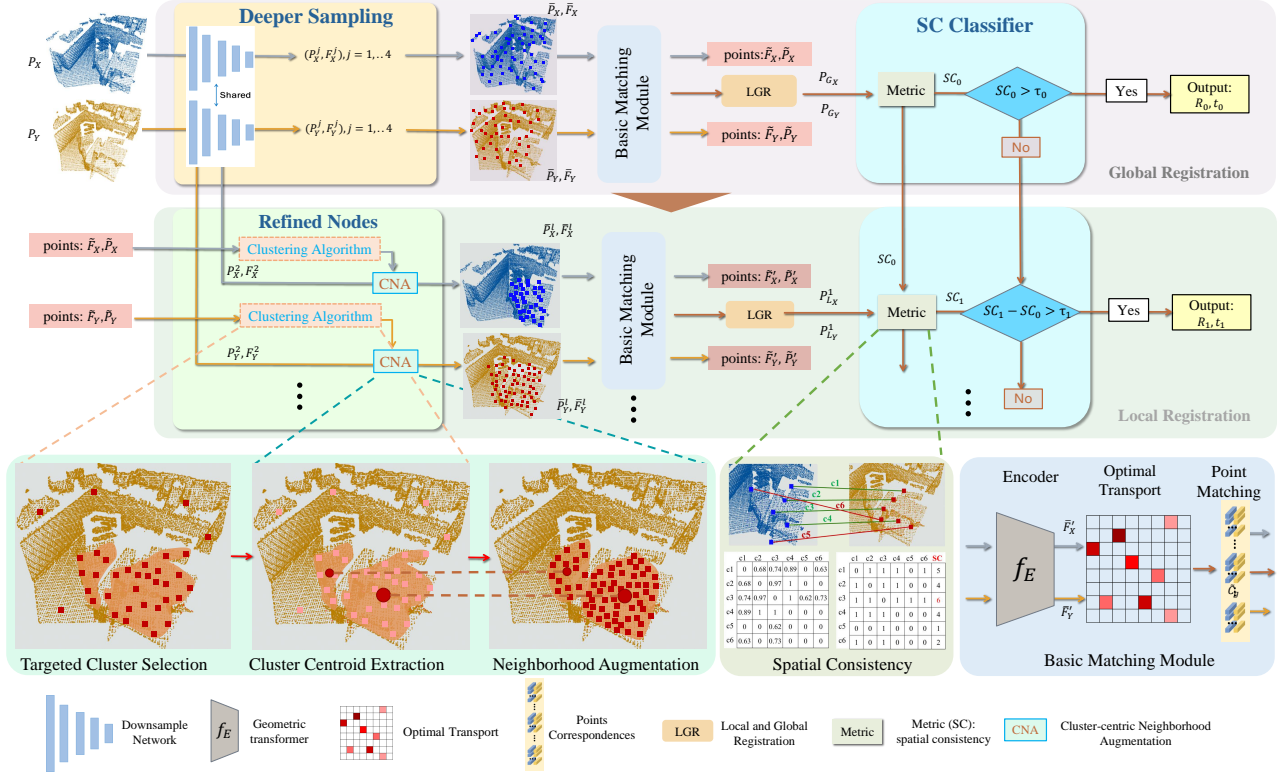


Figure 2: Our DIPR is mainly divided into two parts: global registration and local registration. We first design the Deeper Sampling to downsampling and extract the initial feature. Then, we use the Basic Matching Module to obtain the pairing points \tilde{P}_X and \tilde{P}_Y and the global registration result. Next, the Refined Nodes in the local registration stage clusters the paired points and obtains the new coarse node for local registration. After each registration stage finishes, we design the SC Classifier to determine whether the current result requires further iteration.

cess involves Deeper Sampling for feature extraction, Basic Matching to establish initial correspondences, and Local-to-Global Registration (LGR) to refine these correspondences, ensuring accurate and computationally efficient alignment.

Deeper Sampling. We perform deeper uniform downsampling in the original input data. Inspired by GFNet (Wang et al. 2020), we observe that in point cloud registration tasks, full data may not always be necessary for computations and that only partially accurate pairing relationships can yield satisfactory results. In the global registration stage, we use a minimal number of data points to create a global representation of the point cloud for the global registration, reserving more computational resources for the subsequent local registration phase. We utilize the downsampling network to sample the original point clouds P_X and P_Y to obtain multiple levels of points $P_X^j \in \mathbb{R}^{N_j \times 3}$, $P_Y^j \in \mathbb{R}^{M_j \times 3}$ and their corresponding features $F_X^j \in \mathbb{R}^{N_j \times D}$, $F_Y^j \in \mathbb{R}^{M_j \times D}$ (j represents the number of sampling layers). Our approach allows using different networks for downsampling. In this work, we employ two SOTA backbones, KPConv (Thomas et al. 2019) and the Global Aggregation module from RoITR (Yu et al. 2023b), to demonstrate the effectiveness of our method. Compared with KPConv, Global Aggregation (GA) takes the point cloud coordinates and estimated normals as in-

put, and hierarchically downsamples the original point cloud to coarser nodes through a set of encoder-decoder modules. Due to the addition of normal information, it has better geometric feature representation capabilities, but it also increases the computational complexity. Compared to previous PCR approaches (Yu et al. 2021; Qin et al. 2022; Yu et al. 2023b), we employ a deeper level of sparse downsampling (4 times) during the downsampling process to achieve a sparser global representation, significantly reducing our computational load. We differ from the existing methods in that we use an iterative registration approach. During the subsequent local registration process, we re-obtain coarse nodes around the inliers to avoid reducing the accuracy of the registration results due to the sparse sampling.

Basic Matching Module. We pass the sparse sampled point cloud P_X , P_Y along with its corresponding features \tilde{F}_X , \tilde{F}_Y as coarse nodes into the encoder to learn background geometric information (Qin et al. 2022). The encoder consists of a geometric embedding submodule and multiple transformers. Each transformer includes a self-attention structure, a cross-attention structure and a feedforward network. This process enhances the feature similarity between the two point clouds while improving the feature representation capability. After obtaining the coarse node features \tilde{F}_X, \tilde{F}_Y , we perform the optimal transport to normalize the

node features and measure the pairwise similarity to select the top- k as the coarse correspondence set $C = \{(x'_i, y'_j) \mid x'_i \in \bar{P}_X, y'_j \in \bar{P}_Y\}$.

We employ a coarse-to-fine point matching module to up-sample the correspondence coarse nodes to a denser point set, forming patches $\tilde{P}_X \subseteq P_X^2, \tilde{P}_Y \subseteq P_Y^2$ around the nodes while preserving the pairing relationships between them. Within these corresponding patches, we perform point matching based on feature $\tilde{F}_X \subseteq F_X^2, \tilde{F}_Y \subseteq F_Y^2$, resulting in additional pairwise relationships at the point level, denoted as $\tilde{C} = \{(\tilde{x}_i, \tilde{y}_j) \mid \tilde{x}_i \in \tilde{P}_X, \tilde{y}_j \in \tilde{P}_Y\}$, and the similarity $\tilde{S} = \{\tilde{s}_i \mid \tilde{s}_i \in \mathbb{R}^{|\tilde{C}|*1}\}$ for each pair, which will be further used in the subsequent local registration process.

Local-to-Global Registration (LGR). We use LGR to register the point cloud. LGR first calculates transformations for each patch using its local point correspondences:

$$R_i, t_i = \min_{R, t} \sum_{(\tilde{x}_i, \tilde{y}_i) \in \tilde{C}_i} \tilde{w}_i \|R \cdot \tilde{x}_i + t - \tilde{y}_i\|_2^2 \quad (1)$$

We can obtain $T_i = \{R_i, t_i\}$ by using weighted SVD to solve the above equation in closed form. The match similarity score for each correspondence in \tilde{S} is used as \tilde{w}_i . In all patch transformations, we select the best one as the global transformation and iteratively filter paired points over the global paired points.

$$R, t = \max_{R, t} \sum_{(\tilde{x}_i, \tilde{y}_i) \in \tilde{C}} [\|R_i \cdot \tilde{x}_i + t_i - \tilde{y}_i\|_2 < \tau_t] \quad (2)$$

where $[\cdot]$ is the Iverson bracket, τ_t is the acceptance threshold. After N iterations, we obtain the final pairing relationship $\hat{C} = \{(\hat{x}_i, \hat{y}_j) \mid \hat{x}_i \in \hat{P}_X, \hat{y}_j \in \hat{P}_Y\}$.

Local Registration

After global registration, we use Refined Nodes to obtain new coarse nodes based on the points pairing relationship. In addition, the SC Classifier is used to evaluate the registration results to determine whether to continue after each registration.

Refined Nodes. This module primarily consists of three components: Targeted Cluster Selection, Cluster Centroid Extraction, and Neighborhood Augmentation. During the local registration stage, we aim to narrow down the data scope to reduce computational complexity while avoiding interference from outliers. For pairing relationships \tilde{C} , where the paired points \tilde{x}_i and \tilde{y}_i represent successfully matched points in these two point clouds \tilde{P}_X and \tilde{P}_Y , and the pairing similarity \tilde{S} indicates the degree of similarity between each pair of relationships, which remove a significant portion of point cloud data that could not be paired compared to the original globally sampled point set. The Target Cluster submodule employs an adaptive clustering method, based on the density-based clustering method (DBSCAN) (Ester et al. 1996), to combine paired similarity \tilde{S} and the relative distances within the point sets \tilde{P}_X and \tilde{P}_Y for clustering. The specific implementation is as shown in Algorithm 1.

Algorithm 1: Our Clustering Algorithm Pseudocode

```

Input      :  $P$  - Points cloud data, label - Points labels,  $W$  - Points weights
Parameters:  $\epsilon$  - Radius,  $minPts$  - Density threshold,  $dist$  - Distance
              function
Result     : cluster - Cluster points,  $M$  - Clusters Num
1 CountClusters  $C \leftarrow 0$ ;
2 while True do
3   Distance  $D \leftarrow dist(P, W)$ ;
4   foreach point  $p$  in  $P$  do
5     if label( $p$ ) is undefined then
6       Neighbors  $N \leftarrow RangeQuery(D, p, \epsilon)$ ;
7       if  $|N| < minPts$  then
8         label( $p$ )  $\leftarrow$  Noise;
9       else
10         $c \leftarrow NextClusterLabel$ ;
11        ExpandCluster( $D, N, c, \epsilon, minPts$ );
12 ClustersNum  $M \leftarrow UniqueLabels(label)$ ;
13 if  $M > C$  then
14    $C \leftarrow M, \epsilon \leftarrow \epsilon \cdot 1.1, minPts \leftarrow minPts + 1$ ;
15 else
16   break;
17 cluster  $\leftarrow ExtractCluster(P, label)$ ;

```

By combining \tilde{S} , we can exclude those points with low pairing similarity. Subsequently, in the Cluster Centroid Extraction submodule, we calculate the cluster centers of the clustered point sets P_X^d and P_Y^d to obtain the cluster centers. We compute the distances from each point in the original point set P_X^2 and P_Y^2 to cluster centers and sort them. By ranking the distances, we select the top N_r closest points to achieve Neighborhood Augmentation for the cluster centers. To ensure the efficiency of the local registration stage and the accuracy of the registration results, we maintain the number of refined nodes N_X^r, N_Y^r equal to the number of anchor points \bar{P}_X, \bar{P}_Y used in the global registration. \bar{P}_X^l, \bar{P}_Y^l are then used as the next set of coarse nodes for local registration. The process of getting P_X^c is shown:

$$K(P_X^d, k) = \{p_{x_i}^l \mid p_{x_i}^l \in P_X^2, dist(p_{x_i}^d, p_{x_i}^l) \leq d_k\} \quad (3)$$

Compared to the coarse nodes from the earlier global registration, nodes refined in this manner are more tightly clustered. This refined process also eliminates a significant number of outliers, reducing their impact on the results and computational resource utilization.

Local Matching. The same Basic Matching module is used for the local registration stage. However, this encoder shares the same network architecture as the encoder used in the global stage, but with different parameters. While the global encoder learns sparse global information, the local encoder focuses on learning denser local regions. Using the same encoder for both would lead to a significant decline in network performance due to their differing tasks. The point matching submodule and LGR module remain consistent with those used in the global registration process.

SC Classifier. After each registration stage is completed, we use the classifier to determine whether the registration

result should continue to the next iteration. The classifier serves as the early-exit mechanism to reduce unnecessary computation and dynamically allocate computing resources.

Compared to visual tasks such as object recognition, point cloud registration tasks are challenging to employ deterministic metrics during the inference phase to ascertain whether the current result has achieved the optimal state. We empirically employ spatial consistency SC measurement (Bai et al. 2021) to assess the level of accuracy achieved in the current registration process, allowing us to evaluate the results of each registration attempt and determine whether they have achieved a high level of accuracy. For the pairing relationship \hat{C} , the SC measure is defined:

$$SC_{i,j} = \Phi(d_{i,j}) = \left[1 - \frac{d_{i,j}^2}{\sigma_d^2}\right]_+, d_{i,j} = |d(\hat{x}_i, \hat{x}_j) - d(\hat{y}_i, \hat{y}_j)| \quad (4)$$

where $\Phi(\cdot)$ is a monotonically decreasing kernel function. $[\cdot]_+$ is the $\max(\cdot, 0)$ operation. $d(\cdot, \cdot)$ is the Euclidean distance between two points and σ_d is a distance parameter. (\hat{x}_i, \hat{x}_j) and (\hat{y}_i, \hat{y}_j) are the i, j paired points of correspondence \hat{C} . For the global registration stage, we set the global SC threshold N_g to determine whether the registration can end. For the local registration stage, we set the local SC comparison threshold N_l^i to compare whether the result of the current local registration is better than the previous iteration. If the result of SC is less than N_l^i , it is considered that the results have deteriorated during the iteration process and need to be terminated, otherwise, the next local registration will continue. Using this comparison threshold as the end requirement helps to dynamically determine whether the iteration is over while avoiding the problem of insufficient versatility in different scenarios using a fixed threshold.

The SC Classifier allows the algorithm to promptly end the iteration process without excessive resource consumption. This helps improve efficiency and achieve better registration results within limited computational resources. During the network training process, we inactivate early-exit mechanism by not using the classifier. We assume that before reaching the set maximum number of iterations, each registration result requires the next iteration to ensure that the performance of the network reaches its optimum.

Loss Function. Our loss consists of two components: $L = L_c + \lambda L_p$, with a coarse matching loss L_c and a point matching loss L_p are derived from the registration baseline (Qin et al. 2022). The loss weight λ is used to balance the importance of different loss functions. For a detailed definition, please refer to our supplementary material.

Experiments

Indoor Benchmarks: 3DMatch and 3DLoMatch

Dataset and Metrics. We utilize two popular datasets to evaluate the real-world performance of our method as well as other methods. The 3DMatch (Zeng et al. 2017) dataset is preprocessed and divided into two categories based on the level of overlap: 3DMatch ($> 30\%$ overlap) and 3DLoMatch ($10\% \sim 30\%$ overlap). We use Registration Recall

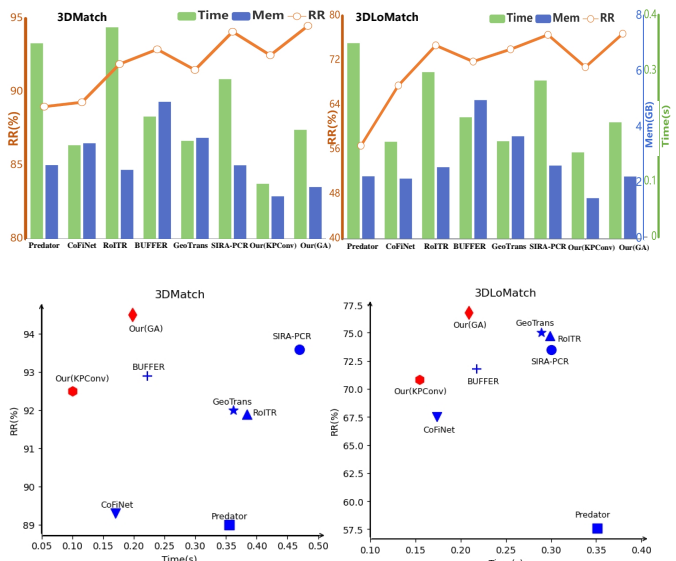


Figure 3: Comparison with existing methods on multiple datasets. Our method achieves SOTA registration accuracy (RR) with much lower time and GPU memory consumption on 3DMatch and 3DLoMatch datasets.

(RR) (most important), Relative Translation Errors (RTE) and Relative Rotation Errors (RRE) to measure the accuracy of registrations. More implementation details are described in our supplementary material.

Results. Our method is compared with eight SOTA methods on registration results (RR), runtime (including data processing, model execution, pose estimation, and total time) and GPU memory usage on the 3DMatch and 3DLoMatch datasets, including CoFiNet, Predator, GeoTrans, REGTR, RoITR, BUFFER, RoReg, and SIRA-PCR. We conducted multiple comparative experiments based on different transformation estimator. Our method employs LGR during the registration process to obtain accurate pairing relationships, thereby eliminating the need for subsequent calculations using RANSAC. As shown in Table 1 and Figure 3, our method (GA for downsampling) achieves SOTA results on both datasets. Compared with methods SIRA-PCR and RoReg with similar results, our method leads the running time of the two data sets by 31% and 26%. In order to prove the effectiveness of our proposed method, we also use the same KPConv-based sampling method as GeoTrans to conduct experiments. The results show that our method (KPConv for downsampling) achieves the fastest running time and second slightest GPU memory usage. The visual results are shown in Figure 4. Our method (GA) achieves lower RMSE errors during the global registration stage compared to GeoTrans. Additionally, scenes that initially fail in registration successfully align after undergoing local registration.

Outdoor Benchmark: KITTI odometry

Dataset and Metrics. The KITTI odometry (Geiger, Lenz, and Urtasun 2012) dataset comprises 11 LiDAR-scanned outdoor driving sequences. Same as 3DMatch, our method is assessed using three key metrics: RRE, RTE and

Table 1: Registration results on 3DMatch and 3DLoMatch datasets. Our method achieves SOTA registration accuracy while using the lowest time and GPU memory consumption. The best and second-best results are marked in bold and underlined respectively to highlight the efficiency and accuracy advantages of our method with different sampling networks and estimators.

Methods	Estimator	Sample	3DMatch						3DLoMatch									
			Time (s)↓			Mem (GB)↓	RR (%)↑	RTE (cm)↓	RRE (°)↓	Time (s)↓			Mem (GB)↓	RR (%)↑	RTE (cm)↓	RRE (°)↓		
			Total	Data	Model					Pose	Total	Data					Model	Pose
Predator (Huang, Gocjic, and Schindler)	RANSAC-50k	1000	0.355	0.267	0.029	0.059	2.680	89.0	6.6	2.015	0.351	0.267	0.028	0.056	2.241	56.7	9.8	3.741
CoFiNet (Yu et al. 2021)	RANSAC-50k	5000	0.170	0.030	0.091	0.049	3.472	89.3	6.4	2.052	0.174	0.030	0.094	0.050	2.159	67.5	9.0	3.180
REGTR (Yew and Lee 2022)	RANSAC-50k	5000	1.283	0.016	0.217	1.050	2.413	86.7	5.3	1.774	1.031	0.015	0.211	0.785	2.264	50.5	8.2	3.005
GeoTrans (Qin et al. 2022)	RANSAC-50k	5000	0.362	0.091	0.079	0.192	3.669	92.0	7.2	2.130	0.289	0.088	0.080	0.121	3.677	75.0	12.6	3.558
RoTR (Yu et al. 2023b)	RANSAC-50k	5000	0.384	0.022	0.214	0.148	2.507	91.9	5.3	1.644	0.299	0.051	0.210	0.067	2.567	74.7	7.8	2.554
BUFFER (Ao et al. 2023)	RANSAC-50k	5000	0.222	0.033	0.186	0.003	4.976	92.9	6.0	1.863	0.218	0.033	0.182	0.003	4.976	71.8	10.1	3.018
RoReg (Wang et al. 2023)	RANSAC-50k	5000	3.490	0.087	0.050	2.353	9.663	93.2	6.3	1.840	3.490	0.087	0.050	2.353	9.662	71.2	9.3	3.090
SIRA-PCR (Chen et al. 2023)	RANSAC-50k	5000	0.469	0.141	0.144	0.184	2.674	93.6	6.3	1.862	0.300	0.140	0.139	0.021	2.627	73.5	8.5	2.846
REGTR (Yew and Lee 2022)	weighted SVD	250	0.229	0.013	0.215	0.001	2.413	92.0	4.9	1.562	0.221	0.014	0.206	0.001	2.328	64.8	7.8	2.767
GeoTrans (Qin et al. 2022)	weighted SVD	250	0.172	0.091	0.079	0.002	3.669	86.5	6.7	2.043	0.170	0.088	0.080	0.002	3.677	59.9	10.2	3.709
BUFFER (Ao et al. 2023)	weighted SVD	250	0.224	0.033	0.189	0.002	4.978	92.1	6.1	1.881	0.214	0.033	0.189	0.002	4.774	70.0	10.0	3.026
RoTR (Yu et al. 2023b)	LGR	all	0.269	0.048	0.214	0.007	2.641	90.9	5.2	1.640	0.266	0.050	0.210	0.006	2.617	73.9	7.4	2.499
GeoTrans (Qin et al. 2022)	LGR	all	0.178	0.091	0.079	0.008	3.669	91.5	6.3	1.808	0.175	0.088	0.080	0.007	3.677	74.0	8.9	2.936
SIRA-PCR (Chen et al. 2023)	LGR	all	0.290	0.141	0.144	0.005	2.674	94.1	5.1	1.539	0.284	0.140	0.139	0.005	2.627	76.6	7.2	2.388
Ours (KPCConv)	weighted SVD	250	0.097	0.048	0.047	0.002	1.547	92.5	6.4	1.917	0.152	0.052	0.098	0.002	1.455	70.3	9.4	3.254
Ours (GA)	weighted SVD	250	0.195	0.012	0.179	0.002	<u>1.883</u>	<u>94.4</u>	6.4	1.755	0.205	0.013	0.190	0.002	2.234	74.4	8.7	3.002
Ours (KPCConv)	LGR	all	<u>0.100</u>	0.048	0.047	0.005	1.547	92.5	6.4	1.897	<u>0.155</u>	0.052	0.098	0.005	<u>1.456</u>	70.8	9.4	3.254
Ours (GA)	LGR	all	0.198	0.012	0.179	0.005	<u>1.883</u>	94.5	6.4	1.772	0.209	0.013	0.191	0.005	2.234	76.8	9.1	2.989

Table 2: Results on KITTI odometry dataset. The best and second-best results are marked in bold and underline, respectively. Our method achieved the best RR and Time.

Method	Time (s)↓	Mem (GB)↓	RR (%)↑	RTE (cm)↓	RRE (°)↓
FCGF (Choy, Park, and Koltun 2019)	7.454	1.788	98.9	6.0	0.39
RegFormer (Liu et al. 2023)	<u>0.205</u>	<u>2.242</u>	<u>99.5</u>	9.7	0.22
Predator (Huang, Gocjic, and Schindler)	0.703	4.634	99.8	6.8	0.26
CoFiNet (Yu et al. 2021)	0.277	3.055	99.8	8.2	0.41
GeoTrans (Qin et al. 2022)	0.251	3.666	99.8	6.2	0.23
BUFFER (Ao et al. 2023)	0.450	5.682	97.5	6.3	0.23
Our(KPCConv)	0.168	2.304	99.8	7.8	0.34

RR which denotes the proportion of point cloud pairs meeting specific criteria (i.e., $RRE < 5^\circ$ and $RTE < 2m$).

Results. We compared our method (KPCConv for downsampling) with FCG, RegFormer, as well as four methods Predator, CoFiNet, GeoTrans, BUFFER and that use KPConv for downsampling on the KITTI dataset. Under the condition of using the same sampling method, our approach achieves SOTA performance on RR while surpassing the second fastest method by over 33% in terms of runtime, and it attains the second smallest result in GPU memory consumption, using less than $2.4GB$. Although FCGF consumes fewer GPU resources, it spends more time on pose estimation, leading to significantly longer runtime compared to other methods. Our network achieves comparable performance in RTE and RRE even though our sampling is sparser, and for the most critical registration metric RR, we achieve the best performance.

Ablation Study

We show the ablation studies of our method (GA) on the 3DLoMatch dataset.

Global and Local Encoder. We test not using two identical encoders in global registration and local registration.

Table 3: Ablation study on 3DLoMatch dataset. The best results are marked in bold.

Module	Model	Time	3DLoMatch RR	RRE	RTE
a. Encoder	1. unique encoder	0.200	74.4	2.990	9.1
	2. Ours	0.209	76.8	2.989	9.1
b. SC Classifier	1. w/o classifier	0.234	72.7	3.032	9.2
	2. Ours	0.209	76.8	2.989	9.1
c. Node	1. random nodes	0.202	74.4	2.969	9.1
	2. average center	0.195	73.4	3.008	9.2
	3. DBSCAN(Ours)	0.209	76.8	2.989	9.1
d. Iteration	1. iteration=0	0.183	73.6	3.010	9.3
	2. iteration=1	0.196	74.4	2.975	9.2
	3. iteration=2	0.201	76.2	3.045	9.2
	4. iteration=3	0.208	76.6	3.056	9.2
	5. iteration=4(Ours)	0.209	76.8	2.989	9.1

For the global registration stage, the data of global sampling points pays more attention to learning the global representation. After multiple downsampling, the greater sparsity between global point clouds leads to larger feature differences between them. For the sampling points used in local registration, more emphasis is placed on learning local information within the neighborhood. Therefore, as shown in Table 3 (a), our method uses two encoders to facilitate enhanced feature learning at different stages, contributing to improved results.

SC Classifier. We implement the early-exit mechanism for the iterative registration process by setting a numerical threshold for first-order spatial consistency (SC).

- Without Classifier.** We test the results without adding the classifier. As can be seen from Table 3 (b), the classifier achieves the purpose of reducing computing resources because it can effectively filter out a large number of simple registration scenarios.
- Different Metrics.** We assess the performance of model after the first local registration using different metrics as the classifier in Table 4, including inlier ratio (IR), normal consistency (NC), second-order spatial consistency

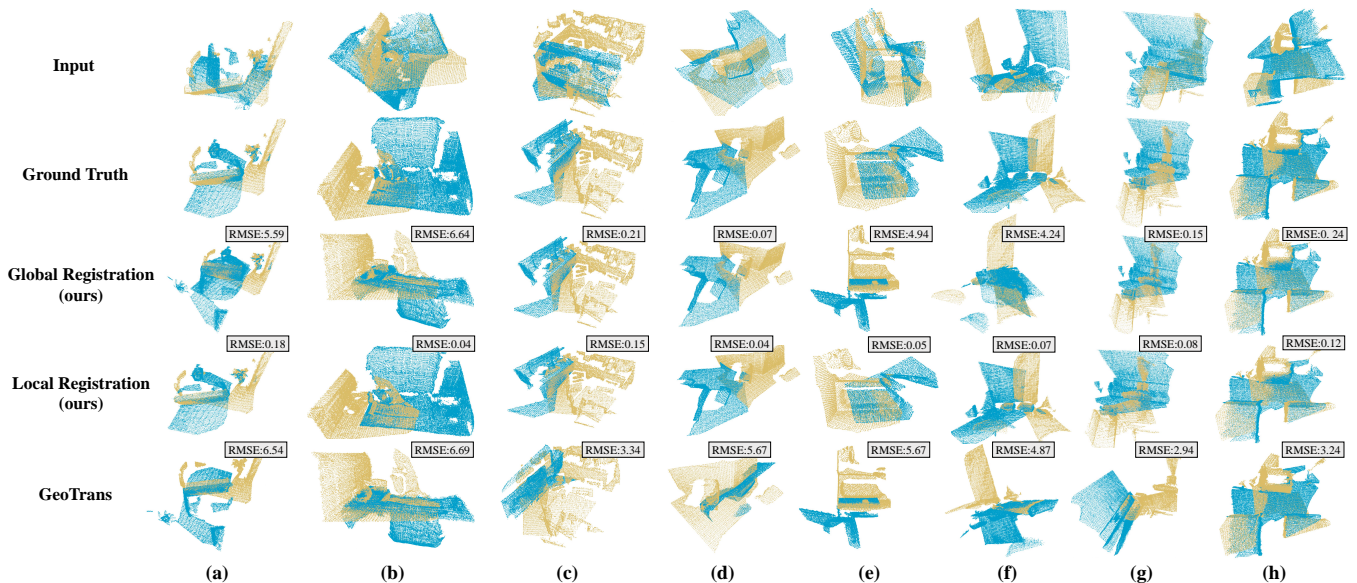


Figure 4: Visualization results of our network for 3DLoMatch (a-d) and 3DMatch (e-h) with global and local registration. Compared to GeoTrans (Qin et al. 2022), our method has similar results in the global registration, and the local registration is further optimized to achieve superior results.

Metrics	N_g	N_l^0	RR	Time
IR	0.30	-	73.4	0.190
NC	150	-	73.5	0.201
SC^2	150	-	72.7	0.209
SC	150	-	73.7	0.200
SC	100	10	74.0	0.194
	150	15	74.4	0.196
	200	20	74.4	0.208

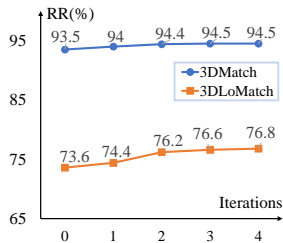


Table 4: Left: Comparison of different metrics and different SC thresholds (N_g). Right: The iteration results on 3DMatch/3DLoMatch demonstrates the effectiveness and stability of our iterations.

(SC^2) and spatial consistency SC . Based on the running time and RR of each metric, SC performs the best.

- Different Thresholds.** We experimented with different global SC thresholds N_g and local SC comparison threshold N_l^i and the results are shown in Table 4. For the local registration stage, We initially set the threshold for the first local SC comparison threshold N_l^1 to 0.1 of the global SC threshold and set the comparison threshold change difference to δN_l^i ($\delta N_l^i=10$ by default), which represents the number of N_l^{i+1} is increased compared to N_l^i each time (i.e., $N_l^i=[15, 25, 35\dots]$).

Refined Nodes. Before performing local registration, we utilize the Refined Nodes module to select new nodes for registration based on the global matched points obtained from the last registration. We compare the DBSCAN clustering algorithm with random sampling and global centers methods, and the results in Table 3 (c) demonstrate that while our method may consume more time, it significantly improves the registration results.

Iteration. In order to prove the effect of iteration of our method, we compare the method global registration Table 3 (d.1) without iteration with the method using local registration multiple times Table 3 (d.2-4) for iteration. Additionally, we plot the iterative results in the line chart shown in Table 4 on the 3DMatch and 3DLoMatch datasets. As the number of iterations increases, the registration results gradually increase starting from 73.6. After the fourth iteration, our method reached the maximum value of 76.8 on the 3DLoMatch dataset. Similarly, we reached the maximum value of 94.5 on the 3DMatch dataset after three iterations and remained unchanged in subsequent iterations. However, during multiple iterations, the RRE continues to increase. This is because, in the process of dynamically finding the registration region, our model continues to reduce the number and region of registration points, which will affect the finer-grained accuracy in some scenes. But it still performs well on the more important metric RR.

Conclusion

We innovatively introduce an efficient Point Cloud Registration via Dynamic Iteration. Our Deeper Sampling reduces significantly the computational complexity of the network, and our Refined Nodes module discovers the inlier concentration region among the paired points for the next registration. The proposed iterative approach dynamically narrows down the registration region to eliminate interference from outliers, and then the iterations are terminated once the registration result meets our SC classifier condition. Extensive experiments demonstrate that our DIPR achieves the best RR result on both 3DMatch and 3DLoMatch datasets while having the advantage of computational efficiency over existing methods.

References

- Ao, S.; Hu, Q.; Wang, H.; Xu, K.; and Guo, Y. 2023. BUFFER: Balancing Accuracy, Efficiency, and Generalizability in Point Cloud Registration. In *Proceedings of the IEEE/CVF Conference on Computer Vision and Pattern Recognition*, 1255–1264.
- Aoki, Y.; Goforth, H.; Srivatsan, R. A.; and Lucey, S. 2019. Pointnetlk: Robust & efficient point cloud registration using pointnet. In *Proceedings of the IEEE/CVF conference on computer vision and pattern recognition*, 7163–7172.
- Bai, X.; Luo, Z.; Zhou, L.; Chen, H.; Li, L.; Hu, Z.; Fu, H.; and Tai, C.-L. 2021. Pointdsc: Robust point cloud registration using deep spatial consistency. In *Proceedings of the IEEE/CVF Conference on Computer Vision and Pattern Recognition*, 15859–15869.
- Chen, H.; Yan, P.; Xiang, S.; and Tan, Y. 2024a. Dynamic Cues-Assisted Transformer for Robust Point Cloud Registration. In *Proceedings of the IEEE/CVF Conference on Computer Vision and Pattern Recognition*, 21698–21707.
- Chen, S.; Xu, H.; Li, H.; Luo, K.; Liu, G.; Fu, C.-W.; Tan, P.; and Liu, S. 2024b. PointRegGPT: Boosting 3D Point Cloud Registration using Generative Point-Cloud Pairs for Training. *arXiv preprint arXiv:2407.14054*.
- Chen, S.; Xu, H.; Li, R.; Liu, G.; Fu, C.-W.; and Liu, S. 2023. SIRA-PCR: Sim-to-Real Adaptation for 3D Point Cloud Registration. In *Proceedings of the IEEE/CVF International Conference on Computer Vision*, 14394–14405.
- Chen, Z.; Sun, K.; Yang, F.; and Tao, W. 2022. Sc2-pcr: A second order spatial compatibility for efficient and robust point cloud registration. In *Proceedings of the IEEE/CVF Conference on Computer Vision and Pattern Recognition*, 13221–13231.
- Chen, Z.; Yang, F.; and Tao, W. 2022. Detarnet: Decoupling translation and rotation by siamese network for point cloud registration. In *Proceedings of the AAAI Conference on Artificial Intelligence*, volume 36, 401–409.
- Choy, C.; Dong, W.; and Koltun, V. 2020. Deep global registration. In *Proceedings of the IEEE/CVF conference on computer vision and pattern recognition*, 2514–2523.
- Choy, C.; Park, J.; and Koltun, V. 2019. Fully convolutional geometric features. In *Proceedings of the IEEE/CVF international conference on computer vision*, 8958–8966.
- Chu, J.; and Nie, C.-m. 2011. Multi-view point clouds registration and stitching based on SIFT feature. In *2011 3rd International Conference on Computer Research and Development*, volume 1, 274–278. IEEE.
- Deng, H.; Birdal, T.; and Ilic, S. 2018. Ppfnet: Global context aware local features for robust 3d point matching. In *Proceedings of the IEEE conference on computer vision and pattern recognition*, 195–205.
- Ester, M.; Kriegel, H.-P.; Sander, J.; Xu, X.; et al. 1996. A density-based algorithm for discovering clusters in large spatial databases with noise. In *kdd*, volume 96, 226–231.
- Fragoso, V.; Sen, P.; Rodriguez, S.; and Turk, M. 2013. EVSAC: accelerating hypotheses generation by modeling matching scores with extreme value theory. In *Proceedings of the IEEE international conference on computer vision*, 2472–2479.
- Geiger, A.; Lenz, P.; and Urtasun, R. 2012. Are we ready for autonomous driving? the kitti vision benchmark suite. In *2012 IEEE conference on computer vision and pattern recognition*, 3354–3361. IEEE.
- Han, Y.; Huang, G.; Song, S.; Yang, L.; Wang, H.; and Wang, Y. 2021. Dynamic neural networks: A survey. *IEEE Transactions on Pattern Analysis and Machine Intelligence*, 44(11): 7436–7456.
- Howard, A. G.; Zhu, M.; Chen, B.; Kalenichenko, D.; Wang, W.; Weyand, T.; Andreetto, M.; and Adam, H. 2017. Mobilenets: Efficient convolutional neural networks for mobile vision applications. *arXiv preprint arXiv:1704.04861*.
- Huang, S.; Gojcic, Z.; and Schindler, M. U. A. W. K. ??? PREDATOR: Registration of 3D Point Clouds with Low Overlap-Supplementary material.
- Huang, T.; Li, H.; Peng, L.; Liu, Y.; and Liu, Y.-H. 2024. Efficient and Robust Point Cloud Registration via Heuristics-guided Parameter Search. *IEEE Transactions on Pattern Analysis and Machine Intelligence*.
- Jiang, H.; Xie, J.; Qian, J.; and Yang, J. 2021. Planning with learned dynamic model for unsupervised point cloud registration. *arXiv preprint arXiv:2108.02613*.
- Li, H.; Zhang, H.; Qi, X.; Yang, R.; and Huang, G. 2019. Improved techniques for training adaptive deep networks. In *Proceedings of the IEEE/CVF international conference on computer vision*, 1891–1900.
- Liu, J.; Wang, G.; Liu, Z.; Jiang, C.; Pollefeys, M.; and Wang, H. 2023. RegFormer: an efficient projection-aware transformer network for large-scale point cloud registration. In *Proceedings of the IEEE/CVF International Conference on Computer Vision*, 8451–8460.
- Meng, Y.; Panda, R.; Lin, C.-C.; Sattigeri, P.; Karlinsky, L.; Saenko, K.; Oliva, A.; and Feris, R. 2020. AdaFuse: Adaptive Temporal Fusion Network for Efficient Action Recognition. In *International Conference on Learning Representations*.
- Pais, G. D.; Ramalingam, S.; Govindu, V. M.; Nascimento, J. C.; Chellappa, R.; and Miraldo, P. 2020. 3dregnet: A deep neural network for 3d point registration. In *Proceedings of the IEEE/CVF conference on computer vision and pattern recognition*, 7193–7203.
- Qi, C. R.; Su, H.; Mo, K.; and Guibas, L. J. 2017. Pointnet: Deep learning on point sets for 3d classification and segmentation. In *Proceedings of the IEEE conference on computer vision and pattern recognition*, 652–660.
- Qin, Z.; Yu, H.; Wang, C.; Guo, Y.; Peng, Y.; and Xu, K. 2022. Geometric transformer for fast and robust point cloud registration. In *Proceedings of the IEEE/CVF conference on computer vision and pattern recognition*, 11143–11152.
- Rusu, R. B.; Holzbach, A.; Blodow, N.; and Beetz, M. 2009. Fast geometric point labeling using conditional random fields. In *2009 IEEE/RSJ International Conference on Intelligent Robots and Systems*, 7–12. IEEE.

- Sarode, V.; Li, X.; Goforth, H.; Aoki, Y.; Srivatsan, R. A.; Lucey, S.; and Choset, H. 2019. Pcnnet: Point cloud registration network using pointnet encoding. *arXiv preprint arXiv:1908.07906*.
- Shen, Y.; Hui, L.; Jiang, H.; Xie, J.; and Yang, J. 2022. Reliable inlier evaluation for unsupervised point cloud registration. In *Proceedings of the AAAI Conference on Artificial Intelligence*, volume 36, 2198–2206.
- Thomas, H.; Qi, C. R.; Deschaud, J.-E.; Marcotegui, B.; Goulette, F.; and Guibas, L. J. 2019. Kpconv: Flexible and deformable convolution for point clouds. In *Proceedings of the IEEE/CVF international conference on computer vision*, 6411–6420.
- Wang, H.; Liu, Y.; Hu, Q.; Wang, B.; Chen, J.; Dong, Z.; Guo, Y.; Wang, W.; and Yang, B. 2023. Roreg: Pairwise point cloud registration with oriented descriptors and local rotations. *IEEE Transactions on Pattern Analysis and Machine Intelligence*.
- Wang, Y.; Lv, K.; Huang, R.; Song, S.; Yang, L.; and Huang, G. 2020. Glance and focus: a dynamic approach to reducing spatial redundancy in image classification. *Advances in Neural Information Processing Systems*, 33: 2432–2444.
- Xu, H.; Ye, N.; Liu, G.; Zeng, B.; and Liu, S. 2022. FINet: Dual branches feature interaction for partial-to-partial point cloud registration. In *Proceedings of the AAAI Conference on Artificial Intelligence*, volume 36, 2848–2856.
- Yang, B.; Bender, G.; Le, Q. V.; and Ngiam, J. 2019. Condconv: Conditionally parameterized convolutions for efficient inference. *Advances in neural information processing systems*, 32.
- Yang, H.; Shi, J.; and Carlone, L. 2020. Teaser: Fast and certifiable point cloud registration. *IEEE Transactions on Robotics*, 37(2): 314–333.
- Yew, Z. J.; and Lee, G. H. 2020. Rpm-net: Robust point matching using learned features. In *Proceedings of the IEEE/CVF conference on computer vision and pattern recognition*, 11824–11833.
- Yew, Z. J.; and Lee, G. H. 2022. Regtr: End-to-end point cloud correspondences with transformers. In *Proceedings of the IEEE/CVF conference on computer vision and pattern recognition*, 6677–6686.
- Yu, H.; Hou, J.; Qin, Z.; Saleh, M.; Shugurov, I.; Wang, K.; Busam, B.; and Ilic, S. 2022. Riga: Rotation-invariant and globally-aware descriptors for point cloud registration. *arXiv preprint arXiv:2209.13252*.
- Yu, H.; Li, F.; Saleh, M.; Busam, B.; and Ilic, S. 2021. Cofinet: Reliable coarse-to-fine correspondences for robust pointcloud registration. *Advances in Neural Information Processing Systems*, 34: 23872–23884.
- Yu, H.; Li, H.; Hua, G.; Huang, G.; and Shi, H. 2023a. Boosted dynamic neural networks. In *Proceedings of the AAAI Conference on Artificial Intelligence*, volume 37, 10989–10997.
- Yu, H.; Qin, Z.; Hou, J.; Saleh, M.; Li, D.; Busam, B.; and Ilic, S. 2023b. Rotation-invariant transformer for point cloud matching. In *Proceedings of the IEEE/CVF Conference on Computer Vision and Pattern Recognition*, 5384–5393.
- Yu, J.; Ren, L.; Zhang, Y.; Zhou, W.; Lin, L.; and Dai, G. 2023c. Peal: Prior-embedded explicit attention learning for low-overlap point cloud registration. In *Proceedings of the IEEE/CVF Conference on Computer Vision and Pattern Recognition*, 17702–17711.
- Zeng, A.; Song, S.; Nießner, M.; Fisher, M.; Xiao, J.; and Funkhouser, T. 2017. 3dmatch: Learning local geometric descriptors from rgb-d reconstructions. In *Proceedings of the IEEE conference on computer vision and pattern recognition*, 1802–1811.
- Zhang, X.; Yang, J.; Zhang, S.; and Zhang, Y. 2023. 3D Registration with Maximal Cliques. In *Proceedings of the IEEE/CVF Conference on Computer Vision and Pattern Recognition*, 17745–17754.
- Zhang, Z.; Sun, J.; Dai, Y.; Zhou, D.; Song, X.; and He, M. 2022. End-to-end learning the partial permutation matrix for robust 3D point cloud registration. In *Proceedings of the AAAI conference on Artificial Intelligence*, volume 36, 3399–3407.
- Zhou, B.; Khosla, A.; Lapedriza, A.; Oliva, A.; and Torralba, A. 2016. Learning deep features for discriminative localization. In *Proceedings of the IEEE conference on computer vision and pattern recognition*, 2921–2929.

Supplementary Materials: A Dynamic Network for Efficient Point Cloud Registration

Supplement of Related Work

Correspondence-based Methods DGR (Choy, Dong, and Koltun 2020) and 3DRegNet (Pais et al. 2020) consider the inlier/outlier determination as a classification problem. MAC (Zhang et al. 2023) developed a compatibility graph to render the affinity relationship between correspondences and construct the maximal cliques to represent consensus sets.

Deep-learned Feature Descriptors PointNetLK (Aoki et al. 2019) and PCRNet (Sarode et al. 2019) integrate PointNet (Qi et al. 2017) into the point registration task and other deep learning methods (Deng, Birdal, and Ilic 2018; Yew and Lee 2020) improve feature extraction module to enhance the capability of feature descriptors. CoFiNet (Yu et al. 2021) leverages a two-stage method, using down-sampling and similarity matrices for rough matching and up-sampling the paired point neighborhood to obtain fine matching. Additionally, RoITR (Yu et al. 2023b) addresses rotation-invariant problems by introducing novel local attention mechanisms and global rotation-invariant transformers. BUFFER (Ao et al. 2023) attempts to improve the computation efficiency, but its performance is mainly reflected in its generalization ability.

Dynamic Neural Networks Compared to static networks, dynamic networks can adapt parameters or structures to different inputs, leading to notable advantages in terms of accuracy, computational efficiency, adaptiveness, etc (Han et al. 2021). In recent years, many advanced dynamic network works have been proposed and mainly divided into three different aspects: 1) sample-wise dynamic networks (Yang et al. 2019) are designed to adjust network architectures and parameters to reduce computation; 2) temporal-wise dynamic networks (Meng et al. 2020) treat video data as a sequence of images to save computation along temporal dimension; 3) spatial-wise dynamic networks (Zhou et al. 2016) exploit spatial redundancy to improve efficiency.

Network Architecture Details

We first introduce the details of the two sampling networks we used, KPConv and Global aggregation, and then introduce the encoder module used in our global and local registration stages.

KPconv Network

We use the KPConv (Thomas et al. 2019) network as our backbone for multi-level downsampling and feature extraction. The specific structure is the same as GeoTrans (Qin

et al. 2022). First, the input point cloud is sampled using grid downsampling with a voxel size of $2.5cm$ on 3DMatch/3DLoMatch and $30cm$ on KITTI. With each subsequent downsampling operation, the voxel size is doubled. We use Deeper Sampling to obtain sparser point clouds, respectively, 5-stage for 3DMatch and 6-stage for KITTI. The numbers of calibrated neighbors used for downsampling are $\{37, 36, 36, 38, 36\}$ for 3DMatch and $\{65, 63, 70, 74, 69, 58\}$ for KITTI. Other settings are consistent with GeoTrans (Qin et al. 2022).

Global Aggregation

We use the Global Aggregation module proposed in RoITr (Yu et al. 2023b) as our downsampling network for multi-level point cloud sampling and initial feature extraction. Different from the RoITr (Yu et al. 2023b), the Global Aggregation we use not only includes the global transformer module, but also includes the complete encoder-decoder structure. The encoder part of the network inputs coordinates, normal vectors and initial features as a pair of triples $\mathcal{P} = (P, N, X)$ and $\mathcal{Q} = (Q, M, Y)$ to downsample the origin points to coarser nodes triples \mathcal{P}' and \mathcal{Q}' . Then, the global transformer aggregates the geometric cues to enhance the features of coarse nodes by the consecutive cross-frame context aggregation. And the decoder module of the network upsample the refined nodes to the original input size through multi-stage upsampling. We also use Deeper Sampling in the network to reduce the number of global registration, while not performing complete upsampling. Here, we set the number of downsampling layers to 5 times, and the number of upsampling layers is 2. Other settings are consistent with RoITr (Yu et al. 2023b).

Geometric Transformer Encoder

We use the Geometric Transformer in GeoTrans (Qin et al. 2022) as our encoder in the global registration stage and local registration stage. Firstly, the encoder receives the features from KPConv and projects them to $d = 256$ for 3DMatch/3DLoMatch and $d = 128$ dimensions for KITTI. For the local encoder, since the features come from the third level of KPConv sampling, the dimensions are from 512 to 256 and 512 to 128 when performing feature projection. Then after three alternations of 'self-attention and cross-attention', the features are obtained and used for pairing point sets through feed-forward networks (FFN).

Implementation Details and Parameters

Our proposed method was implemented by PyTorch. To ensure fairness, we employed the official code and pre-trained

models provided by the baseline methods for comparison. All experiments were performed on the same PC with an Intel Core i7-12700K CPU and a single Nvidia RTX 3090 with 24G memory. We train the model for 40 epochs on both 3DMatch (Zeng et al. 2017) and KITTI (Geiger, Lenz, and Urtasun 2012) with the batchsize of 1. We use an Adam optimizer with an initial learning rate of $1e-4$, which is exponentially decayed by 0.05 every epoch for 3DMatch and every 4 epoch for KITTI. And we set the numbers of down-sampling layers as 5 for the 3DMatch dataset and 6 for the KITTI dataset. The numbers of points in the patch are set to 32 and 64, respectively. Other parameters remain consistent with GeoTrans (Qin et al. 2022).

Refined Nodes Parameters For our refined nodes module, we use the density-based clustering method (DBSCAN) (Ester et al. 1996) combined with the pairing similarity to cluster paired point clouds and form new registration nodes. We set the minimum number of samples for each category to 3 for 3DMatch (Zeng et al. 2017) and 5 for 3DLoMatch and KITTI (Geiger, Lenz, and Urtasun 2012) dataset. The maximum clustering radius are set to gradually increase with the iteration of the registration process. For 3DMatch, the maximum clustering radius is $\{0.125, 0.250, 0.375, 0.500\}$, and for 3DLoMatch, the maximum clustering radius is $\{0.25, 0.30, 0.35, 0.40\}$, while for KITTI it is a fixed value of 30.

SC Classifier Parameters In the inference phase, for the classifier threshold, we set the global SC threshold to 200 for the 3DMatch dataset, and the local SC comparison threshold (limiting the reduction in the number of pairs) to $\{20, 0, -20, -40\}$. Similarly, for 3DLoMatch, we set the global threshold to 150 and the iteration threshold to $\{15, 25, 35, 45\}$, and for KITTI, we set the global threshold to 30 and the iteration threshold to $\{10, 0, -10\}$.

Loss Function

Coarse Matching Loss

We use the overlap-aware circle loss to supervise the point-wise feature descriptors and focus the model on matches with high overlap following GeoTrans (Qin et al. 2022). The overall coarse matching loss is $\mathcal{L}_c = (\mathcal{L}_c^Q + \mathcal{L}_c^P)/2$. Consider a pair of overlapping point clouds P and Q aligned by ground truth transformation. We choose the points $p_i \in P$ that have at least one correspondence in Q to form a set of anchor patches, denoted as \mathcal{A} . For each anchor patch $\mathcal{G}_i^P \in \mathcal{A}$, we consider the paired patches are positive if they share a minimum overlap of 10%, and negative if they have no overlap. We identify the set of its positive patches in Q as ε_p^i , and the set of its negative patches as ε_n^i . The coarse matching loss on P is defined as:

$$\mathcal{L}_c^P = \frac{1}{|\mathcal{A}|} \sum_{\mathcal{G}_i^P \in \mathcal{A}} \log[1 + \sum_{\mathcal{G}_j^Q \in \varepsilon_p^i} e^{\lambda_i^j \beta_p^{i,j} (d_i - \Delta_p)} \cdot \sum_{\mathcal{G}_k^Q \in \varepsilon_n^i} e^{\beta_n^{i,k} (\Delta_n - d_i^k)}] \quad (1)$$

where $d_i^j = \|f_{p_i} - f_{q_j}\|_2$ is the feature distance, $\lambda_i^j = (o_i^j)^{\frac{1}{2}}$ and o_i^j represents the overlap ratio between \mathcal{G}_i^P and \mathcal{G}_j^Q . $\beta_p^{i,j}$ and $\beta_n^{i,k}$ are the positive and negative weights respectively,

Δ_n and Δ_p are the margin hyper-parameters which are set to 0.1 and 1.4. The same goes for the loss \mathcal{L}_c^Q on Q .

Point Matching Loss

During training, we randomly sample N_g ground-truth node correspondences \hat{C}_i^* instead of using the predicted ones. We employ a negative log-likelihood loss on the assignment matrix \bar{C}_i for each sparse correspondences. The point matching loss is calculated by taking the average of the individual losses across all points correspondences: $\mathcal{L}_p = \frac{1}{N_g} \sum_{i=1}^{N_g} \mathcal{L}_{p,i}$. For each correspondence, a set of paired point \mathcal{M}_i is extracted with a matching radius τ . The unmatched points in the two patches are represented by \mathcal{I}_i and \mathcal{J}_i . The individual point matching loss for correspondence \hat{C}_i^* is computed as:

$$\mathcal{L}_{p,i} = - \sum_{(x,y) \in \mathcal{M}_i} \log \bar{C}_{x,y}^i - \sum_{x \in \mathcal{I}_i} \log \bar{C}_{x,m_i+1}^i - \sum_{y \in \mathcal{J}_i} \log \bar{C}_{n_i+1,y}^i \quad (2)$$

Metrics

We use the same metrics for 3DMatch/3DLoMatch and KITTI datasets, namely RTE, RRE, RR respectively.

Relative Translation Error (RTE)

RTE specifically focuses on the translation component of the registration error. It measures the Euclidean distance between the true translation and the estimated translation achieved during the registration process. RTE provides insight into how well the registration algorithm performs in terms of aligning the point clouds along the translation axes.

$$RTE = \|t_{est} - t_{gt}\| \quad (3)$$

where t_{est} and t_{gt} denote the estimated translation vector and ground truth translation vector, respectively. $\|\cdot\|$ represents the Euclidean norm

Relative Rotation Error (RRE)

RRE measures the angular difference between the true rotation and the estimated rotation after point cloud registration. It is a measure of how well the rotational alignment has been achieved.

$$RRE = \arccos\left(\frac{\text{trace}(R_{est}^T R_{gt}) - 1}{2}\right) \quad (4)$$

where R_{est} and R_{gt} denote the estimated rotation matrix and ground truth rotation matrix, respectively. $\arccos(\cdot)$ is the inverse cosine function, $\text{trace}(\cdot)$ represents the trace of the matrix.

Registration Recall (RR)

Registration Recall is a measure of the accuracy of point cloud registration, specifically focusing on the overall transformation quality, considering both rotation and translation.

For 3DMatch/3DLoMatch, RR is computed based on the Root Mean Square Error (RMSE), which is used to measure the distance error between two point clouds. For the set of

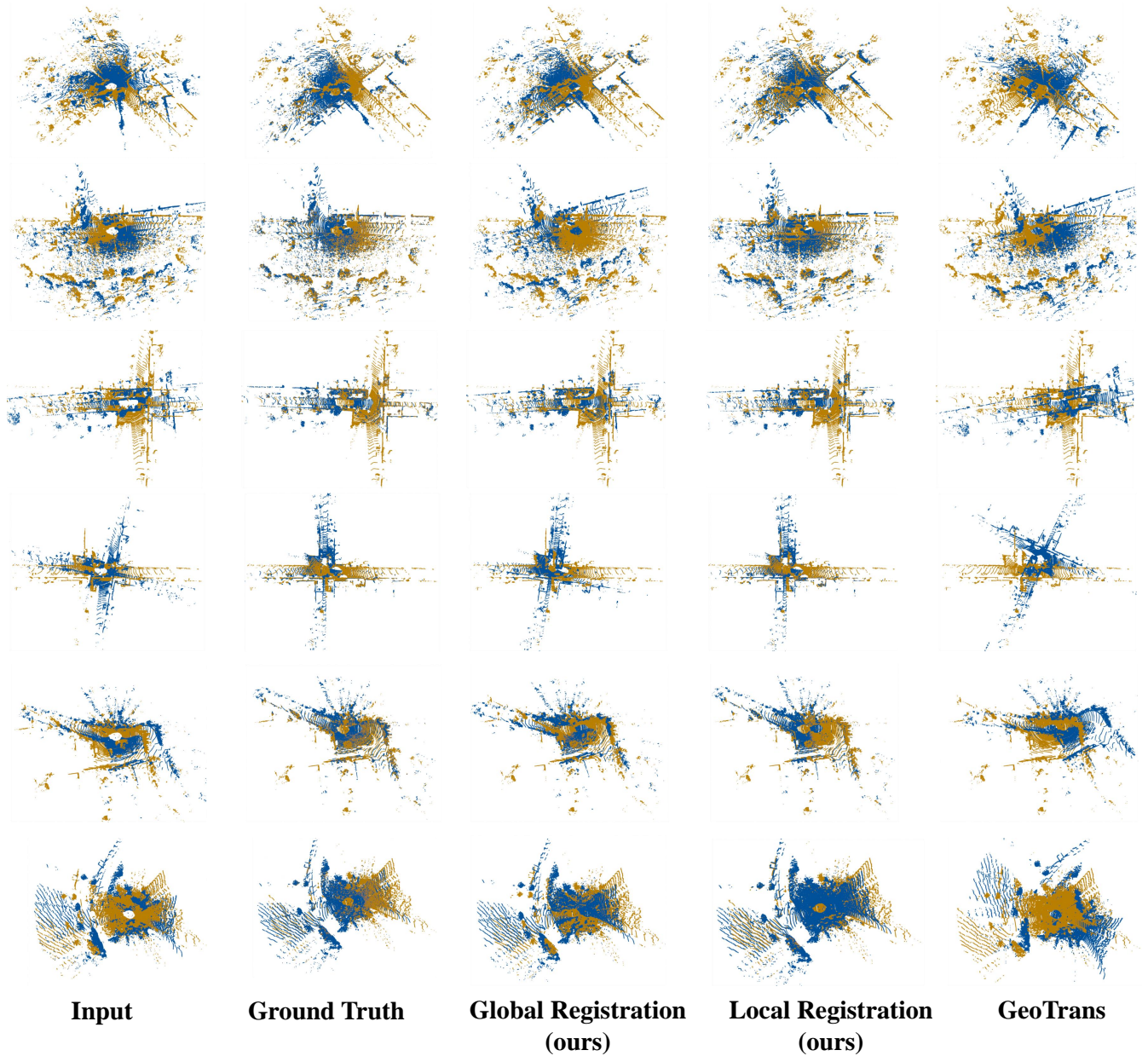


Figure 1: Registration results on KITTI. Our method achieves higher accuracy after local registration and achieves good performance similar to ground truth.

ground truth correspondences C after applying the estimated transformation T_{est} , the calculation formula of RMSE is as follows:

$$RMSE = \sqrt{\frac{1}{|C|} \sum_{(p_i, q_i) \in C} \|T_{est}(p_i) - q_i\|^2} \quad (5)$$

where $|C|$ is the number of correspondence set, p_i, q_i are the i -th pair of paired points in the set of ground truth correspondences C . Lower RMSE values correspond to better

alignment accuracy. RR is defined as:

$$RR = \frac{1}{|C|} \sum_{i=1}^C [RMSE_i < \tau_{RMSE}] \quad (6)$$

where τ_{RMSE} is $0.2m$. For KITTI, RR is defined as the ratio of point cloud pairs for which both the Relative Rotation Error (RRE) and Relative Translation Error (RTE) are below specific thresholds (i.e., $RRE < 5^\circ$ and $RTE < 2m$):

$$RR = \frac{1}{|C|} \sum_i^C [RRE_i < 5^\circ \wedge RTE_i < 2m] \quad (7)$$

Table 1: Ablation study on 3DMatch dataset. The best results are marked in bold.

Module	Model	3DMatch			
		Time	RR	RRE	RTE
a. Encoder	1. unique encoder	0.193	93.5	1.769	6.4
	2. Ours	0.198	94.5	1.772	6.4
b. SC Classifier	1. w/o classifier	0.302	90.4	2.076	7.0
	2. Ours	0.198	94.5	1.772	6.4
c. Node	1. random nodes	0.192	93.6	1.773	6.4
	2. average center	0.190	93.5	1.757	6.3
	3. DBSCAN (Ours)	0.198	94.5	1.772	6.4
d. Iteration	1. iteration=0	0.187	93.5	1.768	6.4
	2. iteration=1	0.191	94.0	1.771	6.3
	3. iteration=2	0.196	94.4	1.771	6.2
	4. iteration=3 (Ours)	0.198	94.5	1.772	6.3
	5. iteration=4	0.201	94.5	1.772	6.3

Additional Experiment Results

We also perform an ablation study on the 3DMatch dataset, as shown in the Table 1. Similar to the experiment on the 3DMatch dataset in the main paper, we verify each block of our model separately and adopt the same experimental settings. The results prove that our default settings achieve the best performance. Besides, we provide the registration results on KITTI in the Figure 1 to show that our method achieves higher accuracy on the KITTI dataset.